Stromal cells regulate malignant B-cell spatial organization, survival, and drug response in a new 3D model mimicking lymphoma tumor niche

Claire Lamaison[1¥], Simon Latour [2,3¥□], Nelson Hélaine[4 ¥], Valérie Le Morvan[2,3], Céline Monvoisin[1], Isabelle Mahouche[2,3], Christelle Dussert[2,3], Elise Dessauge[1], Céline Pangault[1,5], Marine Seffals[6], Léa Broca-Brisson[2,3□], Kévin Alessandri[4□], Pierre Soubeyran[2,3], Frédéric Mourcin[1], Pierre Nassoy[4], Gaëlle Recher[4,**], Karin Tarte[1,5,**] and Laurence Bresson-Bepoldin[2,3,**□]

[¥]: co-first authors

**: co-corresponding authors

[1]UMR S 1236, Univ Rennes, INSERM, Etablissement Français du sang, F-35000, Rennes, France.

[2]Univ. Bordeaux, INSERM, U1218 ACTION F-33076 Bordeaux, France

[3]Institut Bergonié, Comprehensive Cancer Centre, Bordeaux, France

[4]Univ. Bordeaux, CNRS, UMR 5298 LP2N, Laboratoire Photonique Numérique et Nanosciences, Institut d'Optique Graduate School, F-33400 Talence, France

[5]SITI, Pôle de Biologie, CHU Pontchaillou, F-35000, Rennes, France

[6]Univ Rennes1, Inserm, CNRS, UMS Biosit, Core Facility H2P2 Rennes, France

**: Corresponding authors:

laurence.bresson-bepoldin@inserm.fr

karin.tarte@univ-rennes1.fr

gaelle.recher@institutoptique.fr

□ Present addresses:

S Latour: University of Toronto, Institute of Biomedical Engineering, Toronto, Canada

L Broca-Brisson: University Paris-Saclay, CEA, Département Médicaments et Technologies pour la Santé (DMTS), Service de Pharmacologie et Immunoanalyse (SPI), F-91191, Gif-sur-Yvette, France.

K Alessandri: TreeFrog Therapeutics, 33600 Pessac, France

L Bresson-Bepoldin: University of Bordeaux, CNRS, INSERM, Bariton, U1053, F-33000, Bordeaux, France.

ABSTRACT

Non-Hodgkin B-cell lymphomas (B-NHL) mainly develop within lymph nodes as densely packed aggregates of tumor cells and their surrounding microenvironment, creating a tumor niche specific to each lymphoma subtypes. Until now, *in vitro* preclinical models mimicking biomechanical forces, cellular microenvironment, and 3D organization of B lymphomas remain scarce while all these parameters constitute key determinants of lymphomagenesis and drug resistance. Using a microfluidic method based on the encapsulation of cells inside permeable, elastic, and hollow alginate microspheres, we developed a new tunable 3D-model incorporating extracellular matrix and/or stromal cells. Lymphoma B cells and stromal cells dynamically formed self-organized 3D spheroids, thus initiating a coevolution of these two cell types, reflecting their bidirectional crosstalk, and recapitulating the heterogeneity of B-NHL subtypes. In addition, this approach makes it suitable to assess in a relevant *in vitro* model the activity of new therapeutic agents in B-NHL.

INTRODUCTION

Non-Hodgkin lymphoma (NHL) is a group of common hematological malignancies, with the majority of them originating from B cells. Follicular lymphoma (FL) and diffuse large B-cell lymphomas (DLBCL), the two most frequent B-cell NHL (B-NHL) (Smith et al., 2011; Teras et al., 2016), result from the malignant transformation of germinal center (GC) or post-GC B cells. FL are indolent lymphomas characterized by the occurrence of the t(14;18)(q32;q21) translocation combined with additional recurrent somatic alterations (Huet et al., 2018). Two major subtypes of aggressive DLBCL, GC B-cell (GCB) and activated B-cell (ABC)-DLBCL, have been identified using gene expression profiling, reflecting their putative cell of origin and molecular alterations (Alizadeh et al., 2000). Despite a better understanding of the pathophysiology of these tumors, frontline therapy remains based on a combination of conventional chemotherapies such as CHOP (Cyclophosphamide, Hydroxydaunorubicin, Vincristine and Prednisone) and a monoclonal antibody against CD20. Nonetheless, 30–40% of DLBCL patients develop relapse or have refractory disease that cannot be cured with the standard immunochemotherapy (Sehn and Gascoyne, 2015). In addition, FL remains essentially an incurable disease and about 20% of patients progress or relapse in the first 2 years following treatment initiation, with a dismal prognosis (Huet et al., 2018).

It is now widely accepted that tumors constitute a complex ecosystem composed of many cell types regulated by biological, structural, chemical, and mechanical cues, that altogether participate in the effectiveness of therapeutic molecules (Bissell and Radisky, 2001). The tumor microenvironment of B-cell lymphomas contains highly variable numbers of immune cells, stromal cells, blood

vessels, and extracellular matrix (ECM) and the interplay between these elements produces a tumor niche specific to each lymphoma subtypes (Scott and Gascoyne, 2014; Verdière et al., 2018). FL exhibits a high dependence on a GC-like microenvironment where immune and stromal cells support survival, proliferation, and migration of malignant B cells. In turn, FL cells modulate the phenotype and function of their surrounding microenvironment. In particular, FL-infiltrating stromal cells are engaged in a bidirectional crosstalk with malignant B cells within infiltrated lymph nodes and bone marrow (Guilloton et al., 2012; Pandey et al., 2017). Conversely DLBCL have been proposed as less dependent on lymph node microenvironment but specific stromal signatures have been shown to impact DLBCL prognosis (Fowler et al., 2016; Scott and Gascoyne, 2014). Importantly, studies exploring functional interactions between lymphoma B cells and stromal cells have been essentially performed in 2D *in vitro* culture models whereas biomechanical forces and 3D organization emerged as key determinants of lymphoma pathogenesis and drug resistance.

In vitro, 2D culture of cell lines is the model mainly used to screen new molecules. However, this constitutes an “ideal” model where nutrients, oxygen, and drugs reach freely all cells. In addition, these cell cultures do not consider the spatial architecture of tissues, and lack microenvironment and ECM identified as tumor safety guards from chemotherapies. In this context, multicellular spheroids or tumor organoids represent promising models allowing high-throughput screening of anti-cancer drugs in versatile systems mixing several cell types and ECM components. While 3D culture models are increasingly developed for solid cancer (Clevers, 2016), their transfer to lymphoma modeling is still limited and includes: i) multicellular aggregates of lymphoma cells obtained using hanging drop method, which are useful

for testing drug efficacy but do not account for the effect of cell-cell and cell-ECM interactions (Decaup et al., 2019; Gravelle et al., 2014), ii) 3D lymphoma organoid models integrating lymphoid-like stromal cells or integrin-specific binding peptides to recapitulate more accurately lymphoma microenvironment, but difficult to handle and low throughput (Tian et al., 2015).

In the present study, we aimed at providing a 3D lymphoma model that both integrates interactions between stromal cells and lymphoma B cells and is amenable to high throughput screening. Using a microfluidic method based on the encapsulation of cells inside permeable, elastic, and hollow alginate microspheres (Alessandri et al., 2013), we developped a new tunable 3D model incorporating ECM and/or stromal cells. We showed that lymphoma B cells and stromal cells form 3D spheroids whose internal architecture is driven by self-organization, thus initiating a bidirectional crosstalk and a co-evolution of these two cell types, recapitulating the heterogeneity of B-NHL subtype. In addition, this approach makes it possible to assess drug efficacy in a relevant *in vitro* B-NHL model.

RESULTS

1) B-NHL cell lines form cohesive spheroids in scaffold-free alginate capsules

To produce spheroids from lymphoma B-cell lines, we used the cellular capsule technology, initially developed to generate spheroids from solid cancer tumor cells (Alessandri et al., 2013, 2016). Three B-NHL cell lines have been selected for encapsulation as representative models for GCB-DLBCL (SU-DHL-4), ABC-DLBCL (HLY1) and FL (DOHH2). From image-based analysis (N=656), the mean of the capsule diameter distribution was 215.9 ± 1.3 µm and the capsules contained an average of 18.2 ± 0.8 cells/ capsule (N=48) (Figure S1). During the first 11 days, SU-DHL-4 and HLY1 proliferated and aggregated to form spheroids. Alike the terminology used for 2D cultures, we called '3D confluence', the stage when cells filled up the capsule and reached the internal wall of the alginate shell. Contrastingly, DOHH2 cells were not able to grow and form spheroids even after 17 days (Figure 1A) suggesting their requirement of a supportive microenvironment. Cell survival in SU-DHL-4 and HLY1 spheroids was evaluated at various culture time points using propidium iodide labelling. Upon spheroid dissociation and flow cytometry quantification, we found that the percentage of dead cells remained as low as 20-30% during the first week in culture and then increased to about 60% after 8 to 12 days (Figure 1B). As a corollary, EdU staining revealed that the early stages of spheroid growth were characterized by a high proliferation rate while post-confluent stages exhibited a significant decrease in cell proliferation concomitant with cell death increase (Figure S2). To determine whether this survival decrease was associated with the formation and growth of a dead cellular core, as observed in solid tumor spheroids (Däster et al., 2016; Sutherland, 1988), we performed immunostaining for

cell proliferation (Ki67) and cell death (cleaved caspase 3). Besides an increased cell death after confluence (Figure 1B and Figure S2), neither Ki67 nor cleaved-caspase-3 regionalization was detected at prior or after 3D confluence (Figure 1C).

To check that the capsule content was not only a confined cell suspension but formed truly cohesive spheroids, the alginate shell was dissolved in PBS containing 1 mM EGTA. As shown in figure 2A (and movie 1), the integrity of the cellular aggregates observed after confluence was maintained upon capsule dissolution, suggesting that 3D culture may induce the secretion of cohesive ECM. We thus compared by immunofluorescence the expression of laminin, fibronectin, and collagen I, three ECM components expressed in secondary lymphoid organs (Chen et al., 2012; Sobocinski et al., 2010), between cells cultured in suspension (2D) or in capsules (3D). SU-DHL-4 already expressed collagen 1 in 2D culture and upregulated laminin and fibronectin in 3D spheroids. Conversely, HLY1 displayed similar laminin expression in 2D and 3D cultures but increased fibronectin and collagen 1 in 3D spheroids (Figure 2B). Altogether these data argue for a promotion of ECM expression in 3D cultures of lymphoma cells.

Altogether, these data show that the cellular capsule technology is a valuable approach to produce cohesive lymphoma spheroids from DLBCL.

2) Tumor B-cell and stromal cell co-encapsulation and 3D self-organization promote spheroid growth

Since B-NHL are organized as mixed aggregates of tumor cells and lymphoma-supportive non-malignant components (Verdière et al., 2018), we decided to aim for a more physiopathological model by introducing lymphoid stromal cells isolated from human tonsils (Tonsil Stromal Cells, TSC) (Ame-Thomas et al., 2007)

and ECM components (Matrigel). We observed that lymphoma cell growth, evaluated by cell counting, was differentially regulated by the presence of ECM and stromal cells. Indeed, while the presence of stromal cells had no significant effect on HLY1 spheroid growth, they significantly increased the growth kinetic of SU-DHL-4 spheroids, and they even promoted DOHH2-derived spheroid formation and growth, which were not achieved in the absence of TSC (Figure 3A). These results suggest that our 3D model recapitulates the high TSC-dependence of FL B cells whereas DLBCL exhibit a more variable dependence (Ciavarella et al., 2018).

We next sought to decipher how stromal cells play a supportive role on DOHH2 spheroid formation. DOHH2 cells were co-encapsulated with TSC in the presence or absence of a layer of Matrigel anchored to the inner wall of the capsules (Alessandri et al., 2016). In the absence of Matrigel, the capsule wall remained cell-repellent and stromal cells formed clusters inside the capsules but were unable to induce DOHH2 spheroid growth (Figure 3B and C). In contrast, in the presence of Matrigel, TSC spread onto ECM, leading to the formation of a ramified 3D network of stromal cells, that subsequently supported B cell proliferation (Figure 3D and movies 2-3).

We then monitored the stromal cell network dynamic by imaging capsules after 2, 24, 48, 72, and 96h of culture using confocal microscopy (Figure 4A). By solely focusing on stromal cells, we performed 3D+time image analysis and measured sphericity and branchness that both characterized the evolution of the stromal cell network complexity. High sphericity index indicated a compact morphology of the stromal network, thus offering a limited surface of interaction with B cells. Conversely, high branchness index was associated to a ramified network that increased the probability of B cell-stromal cell physical contacts. Stromal cell morphology was significantly modified as early as 24h after encapsulation, as revealed by the

opposite variations of the sphericity and branchness indexes (Figure 4B and C). In addition, after a rapid initial change, both parameters underwent a slower but continuous evolution in time in the same correlated manner, indicating that the increased branching architecture of the stromal network was not a disorganized and randomly observed feature but was sustained by a self-organization process (Figure 4D).

3) ***Microencapsulated 3D co-cultures recapitulate phenotypic features of B lymphomas***

We decided to focus on the 3D TSC-DOHH2 co-culture to investigate the stromal/B-cell bidirectional crosstalk. Previously, we have demonstrated that FL B cells could contribute to the commitment of mesenchymal precursors into lymphoid-like differentiation (at least partly through the secretion of TNFα (TNF)) (Ame-Thomas et al., 2007; Guilloton et al., 2012). Interestingly, we revealed that 3D cell co-cultures induced a stromal cell phenotype similar to that observed *in situ* in FL lymph nodes (Figure 5). More specifically DOHH2 induced podoplanin (PDPN) expression in stromal cells while this was not the case in 2D co-cultures in which only the treatment of TSC cells with a combination of TNF and lymphotoxin α1β2 (LT), the two factors involved in lymphoid stroma differentiation, was able to trigger stromal PDPN expression (Figure 5 and Figure S3). Within spheroids, stromal cells thus acquired characteristics mimicking those observed *in situ*, suggesting that 3D spatial organization is an added value to recapitulate the pathophysiology of lymphoma tissues.

We next studied the gene expression profile (GEP) of DOHH2 cells cultured for 10 days either in monoculture in 2D (noted 2D), or in co-culture with TSC in 2D or 3D

(respectively noted 2D + TSC and 3D + TSC). Data were then compared with the GEP of purified FL B cells and normal tonsil centrocytes (CC) obtained by Affymetrix microarrays. Expression of 37 genes involved in several transduction pathways including NF-κB cascade, migration signaling, cell cycle/quiescence, and apoptosis, was studied by RT-qPCR (Table 1, Figure S4). Analyses revealed a shift in GEP of B cells cultured in 3D compared to cells cultured in 2D with or without TSC (Figure 6 A). In particular, we observed that the expression of *CDKN1A* and *CDKN1B,* two regulators of cell quiescence (Heldt et al., 2018; Sgambato et al., 2000; Zhang et al., 2013), was similarly up regulated in 3D vs 2D co-cultures and in FL-B cells vs GC B-cells (Figure 6B). Moreover, *BCL2* was upregulated in DOHH2 after the 3D co-culture and was highly expressed in FL B cells (Figure 6C).

The hypoxic tumor environment has been often reproduced in 3D tumor *in vitro* models (Benien and Swami, 2014). We confirmed this observation in our lymphoma 3D model, since both the upstream HIF1A transduction pathway regulator (*EGLN1*) and some HIF1A target genes (*VEGF, CXCR4*) were upregulated compared with 2D co-culture condition, reflecting, at least in part, the expression pattern obtained in FL B cells compared with normal CC (Figure 6D and E).

FL is a disseminated disease and we thus sought to determine the impact of 3D architecture on the expression of genes involved in cell confinement or cell migration. Interestingly, *RGS13*, known to limit GC size and GC B-cell number by interfering with CXCL12 and CXCL13 signals (Hwang et al., 2013), was specifically downregulated in 3D co-cultures and FL B cells. Conversely, *CXCR4* expression was similarly upregulated in FL-spheroids and FL B cells (Figure 6E).

Activation of the NF-κB pathway has been extensively described in B-NHL (Kennedy and Klein, 2018), leading us to investigate the expression of this pathway

in our 3D model. Our analyses revealed an upregulation of the noncanonical (*RELB*) NF-κB pathway in spheroids compared to 2D co-cultures. Concomitantly, the expression of *TNFAIP3,* a negative regulator or the canonical NF-κB pathway, as well as that of *BCL21A* and *CFLAR*, two target genes of NF-κB, were increased in 3D compared to 2D co-cultures (Figure 6F). These results suggest that a functional non-canonical NF-κB pathway is activated in FL-spheroids.

Collectively, these results suggest that the co-culture of DOHH2 with TSC in 3D exhibits high degree of similarity with FL biopsies and partly mimics the lymphoma niche.

4) B-NHL sensitivity to chemotherapy in 3D vs 2D cell culture

We wondered whether the 3D architecture could alter the drug response of lymphoma B cells. For that purpose, we evaluated the effect of doxorubicin, one of the components of the classical polychemotherapy used in B-NHL (CHOP), on the cell death of B-NHL cell lines cultured in 2D or 3D in the absence or presence of stromal cells. As shown in Figure 7A, we observed that the induction of apoptosis by doxorubicin tested at a concentration corresponding to its EC50 for the different cell lines (Figure S5), was abolished or significantly decreased in cells cultured in 3D compared to 2D. Based on our results showing that *BCL2* expression was upregulated in FL spheroids, we then tested the effect of a BCL2 inhibitor. ABT-199 induced massive cell death in DOHH2 co-cultured in 2D with or without stromal cells, as well as in 3D co-cultures, suggesting that malignant B cells retained their dependence on BCL2 expression for survival (Figure 7B).

Altogether, these results reveal that our 3D lymphoma model may be useful to perform precision medicine or drug screening.

DISCUSSION

Lymphomas develop as complex cell structures including tumor cells and their microenvironment within mechanically constraint lymph nodes (LN). Previous lymphoma spheroid models incorporating only malignant B cells (Decaup et al., 2013; Gravelle et al., 2014) have already suggested that the 3D cell architecture is a key feature for the regulation of lymphoma growth and therapeutic response. LN are highly dynamic structures expanding and becoming mechanically stiff under immune cell recruitment and proliferation, whereas immune response resolution is associated with LN contraction and return to a baseline of mechanical softness (Fletcher et al., 2015). LN mechanical properties rely on several determinants including the external constraint of the capsule and the internal tension created by the TSC network of specialized myofibroblasts able to produce and contract ECM. Moreover, mechanosensing has been recently demonstrated to control T-cell activation and metabolism (Meng et al., 2020) together with mechanical forces are involved in TCR (Hu and Butte, 2016) and BCR (Apoorva et al., 2018) signaling. Mouse models of FL and DLBCL cannot entirely recapitulate the biology of these tumors (Ramezani-Rad and Rickert, 2017) and, due to their inherent complexity and cost, they are not suitable to study specific cellular interactions contributing to the organization of lymphoma cell niche or to perform drug screening. The development of 3D lymphoma models including mechanical constraints is therefore of particular relevance to advance the understanding and treatment of these neoplasia. In the present work, we adapted a microfluidic approach to recapitulate the lymphoma microenvironment in hollow, permeable alginate shells, forming high-throughput (~5000/s), size-controlled, and easy to handle spheroids (Alessandri et al., 2013). Such a strategy is ideally suited for drug testing and the versatility of the technique allows generating

3D monocultures (i.e. from tumor B cells only) or co-cultures with human stromal cells, and to evaluate the impact of ECM.

First, the proliferation of malignant B cells alone within spheroids results in cohesive multicellular aggregates promoted by the over-secretion of ECM in 3D compared to 2D cultures. Although expression and secretion of ECM have been mainly described in stromal cells, we demonstrated here that lymphoma B cells display a similar ability, as already proposed for normal plasmablasts (Della-Torre et al., 2020) and plasma cells (Tancred et al., 2009), or leukemic B cells (Mikaelsson et al., 2005). How ECM expression is regulated remains unclear. We could however hypothesize that it may originate from the activation of a mechanotransduction pathway as already described in other cell types (Coplen et al., 2003; He et al., 2004). Remarkably, alginate capsules are elastic, meaning that cell growth past confluence dilates the capsule, which conversely applies a compressive force onto the spheroid (Alessandri et al., 2013). Although not investigated in depth, we qualitatively observed that the cohesion of spheroids was stronger for post-confluent capsules, which would support this mechanotransduction hypothesis.

Second, as previously reported using other 3D models, some B-cell lines, including DOHH2, were unable to grow and form spheroids when maintained alone in capsules, reproducing the strong dependency of FL on their niche for survival and growth. Guided by our previous studies showing that lymphoid-like stromal cells have a supportive effect on FL B cells (Ame-Thomas et al., 2007; Gallouet et al., 2014; Guilloton et al., 2012), we added TSC to generate hybrid stroma-tumor 3D lymphoma models. Interestingly, our 3D model reproduced the different levels of NHL microenvironment dependency, mimicking the biology of aggressive versus indolent lymphomas (Scott and Gascoyne, 2014). By contrast with other 3D culture

317 approaches that consist in embedding cells in an ECM scaffold (Gravelle et al., 2014;
318 Purwada et al., 2015; Sabhachandani et al., 2019; Tian et al., 2015), our alginate
319 spheroid model allows cell motions and interactions, leading to an early self-
320 organization of a stroma-tumor B cell network that could organize localized 3D niches
321 promoting cell interactions within the spheroids. Besides favoring or allowing
322 malignant B-cell growth, the 3D co-culture was also associated with coevolution of
323 stromal cells. In particular, TSC displayed increased podoplanin expression in 3D,
324 mimicking the phenotype of FL-infiltrating stromal cells (Pandey et al., 2017),
325 whereas such induction was not observed in 2D co-culture. Podoplanin is a
326 transmembrane glycoprotein known to mediate the lymphoid stromal cell contractile
327 function within LN (Astarita et al., 2015). It is thus tempting to speculate that
328 podoplanin upregulation could contribute to the regulation of spheroid mechanical
329 constraints. Production of TNF by malignant B cells has been proposed as a key
330 mechanism of their dynamic interaction with stromal cells, leading to the upregulation
331 of podoplanin, CCL2, and IL-8 in 2D culture conditions *in vitro* (Guilloton et al., 2012).
332 However, neither TNF nor LT were found upregulated in DOHH2 maintained in 3D
333 culture (data not shown), confirming a recent work performed on composite hydrogel-
334 based lymphoma spheroids (Sabhachandani et al., 2019), suggesting that other
335 soluble factors, but also 3D architecture and spatial constraints could contribute to
336 the reprogramming of stromal cells.

337 Overall, the analysis of B-cell gene expression profile within spheroids
338 revealed a profound shift associated with the transition from a 2D to a 3D context,
339 mimicking the phenotype of primary FL B cells. The drop of B-cell proliferation that
340 took place when cells filled the capsule was associated with an upregulation of
341 quiescence genes also strongly expressed by FL B cells in agreement with their

indolent phenotype. Even in the absence of a necrotic core within spheroids, the increase of *EGLN1* and *VEGF* expression could reflect a response to hypoxia, a process associated with a limitation of energy consumption through reduction of cell proliferation and DNA repair (Goda et al., 2003; Koshiji et al., 2004). Such association of response to hypoxia and quiescence has been previously described in a 3D model where spheroids were generated by the hanging drop method with lymphoma B cells alone (Gravelle et al., 2014). Interestingly, BCL2 was found upregulated in 3D spheroids and has been previously shown to display anti-proliferative effects in normal and malignant B cells (Tellier et al., 2014; Zinkel et al., 2006), suggesting that it could contribute to the decrease of cell proliferation. Even if the t(14;18) is the main driver of BCL2 deregulation in FL, BCL2 expression shows a high level of inter- and intra-tumoral heterogeneity and is correlated with IgH expression and NF-κB activation (Barreca et al., 2014; Heckman et al., 2002). Accordingly, we highlighted an upregulation of *RELB* and NF-κB target genes in 3D co-cultures, indicating that the NF-κB pathway was activated in lymphoma spheroids. Of note, a recent study revealed that fluid shear stress upregulates BCR expression and signaling in ABC-DLBCL (Apoorva et al., 2018), suggesting that engagement of BCR/NF-κB/BCL2 loop by biophysical forces could be a general feature of B-cell lymphomas. Finally, we described in our 3D model an upregulation of *CXCR4*, previously associated with FL B-cell migration, adhesion, and survival. Together with the reduction of *RGS13* involved in the organization of GC into dark and light zones and the limitation of GC size (Hwang et al., 2013; Shi et al., 2002), this could reproduce some of the factors sustaining FL dissemination and will require further investigations.

366 BCL2 expression is a key determinant of response to therapy in FL patients
367 (Barreca et al., 2014). Moreover, the 3D-induced drug resistance has been already
368 reported in solid cancers and hematological malignancies (Desoize, 2000; Gravelle et
369 al., 2014; Tian et al., 2015). We confirmed here that the sensitivity to doxorubicin
370 dramatically dropped when cells were cultured in 3D compared to 2D in all
371 investigated B NHL cell lines. By contrast, the pro-apoptotic activity of ABT-199,
372 mediating the dissociation of BCL2 with the proapoptotic BH3 only proteins, was
373 maintained in 3D co-cultures despite BCL2 upregulation suggesting that ABT-199
374 might be considered as a good alternative for FL patient treatment. More generally,
375 the cellular capsule technology adapted for lymphoma 3D culture seems a useful tool
376 to screen new therapeutic approaches.

377 In summary, we report the development of a new lymphoma 3D model,
378 including stromal cells and ECM, and recapitulating the dynamic crosstalk between
379 tumor cells and their supportive microenvironment. The versatility of this high-
380 throughput platform makes it possible to evaluate the role of various ECM
381 components, stromal cell subtypes, and soluble factors on the spatial organization
382 and function of the lymphoma niche. Moreover, this approach is particularly suitable
383 for the testing of new therapeutic agents in B-NHL.

384

MATERIALS AND METHODS

Reagents and antibodies

Alginic acid sodium salt from brown algae, D-Sorbitol and $CaCl_2$ hexahydrate, EGTA, paraformaldehyde were supplied by Merck (Fontenay sous bois, France). Matrigel was provided by Corning (UGAP, France). Propidium iodide and Phalloidin-Alexa 594 were from Thermo Fisher Scientific (Courtaboeuf, France). Hoechst 33258 and ABT-199 were purchased from Tocris Bioscience (Lille, France). The comprehensive cancer center pharmacy department of the Institut Bergonié kindly provided doxorubicin. APC Annexin V was from BD Biosciences (Le pont de Claix, France).

Rabbit polyclonal anti-laminin, rabbit polyclonal anti-fibronectin, rabbit monoclonal anti-human collagen I and chicken polyclonal anti-GFP antibodies were supplied by Abcam (Paris, France). Mouse anti-human CD20 APC-H7 and mouse anti-human CD73 PE were from e-Bioscience (Thermo Fisher Scientific). Monoclonal mouse anti-human Ki67 was from Dako Agilent Technologies (Les Ulis, France) and rabbit polyclonal anti-cleaved caspase 3 antibody was provided by Cell Signaling Technology (Ozyme, Saint Cyr l'école, France). All Alexa-conjugated secondary antibodies were purchased from Thermo Fisher Scientific.

Encapsulation procedure

Cell encapsulation was performed by adapting the protocols from (Alessandri et al., 2016; Doméjean et al., 2016; Trushko et al., 2020). Briefly, it includes the fabrication of the device, the preparation of the solutions and the operation itself for cellular capsules formation.

First, the microfluidic device was printed with EnvisionTEC Micro Hi-Res Plus 3D printer (Arketyp3D, Le Raincy, France) using the resin HTM140V2 (EnvisionTEC), with the following printing parameters: burn-in range thickness 400µm, base plate of 300µm, and exposure time 3000ms. The printed device was washed using propanol and air-dried. In parallel, a glass capillary was pulled using a micropipette puller (P30, Sutter Instrument, Micro Mecanique SAS, Saint Germain en Laye, France), then cut and polished with micro-abrasive films (1µm grain, 3M) to reach the desired tip diameter (typically between 130 and 180 µm). This glass tip, which serves as a nozzle for the encapsulation device, was hydrophobized (1H,1H,2H,2H-Perfluorooctyltrimethoxysillane, ABCR) following standard protocols (Perret et al., 2002) and glued to the exit of the microfluidic plastic device with epoxyglue EA M-31CL (Loctite).

To run an encapsulation, the microfluidic device is connected to three syringes (10MDR-LL-GT SGE, Analytical Science, Milton Keynes, UK) mounted on pumps (Nemesys, Cetoni GmbH, Korbussen, Germany) for flow rate control. Three different solutions are injected into the three coaxial cones of the device. The outermost cone contains the alginate solution, which is prepared by dissolving 2% wt/vol sodium alginate (Protanal LF200S) in water and by adding 0.5mM SDS surfactant (VWR International, Fontenay sous bois, France). The solution was filtered at 1µm (glass filters, Pall Life Science) and stored at 4 °C. The intermediate cone contains a 300 mM sorbitol (Merck) solution. The innermost cone contains cells suspended in a sorbitol solution or cells/Matrigel/sorbitol solution (when ECM is needed) in a ratio of 2:1:2 (v/v). Lymphoma B cells lines were taken from cell suspension routinely cultured while adherent stromal cells were detached from the culture flask with trypsin-EDTA (Thermo Fisher Scientific). After rinse, cells were centrifuged and

434 counted. For encapsulation of lymphoma cells or stromal cells only (mono-culture), a
435 suspension of 2×10^6 cells were resuspended in culture DMEM (Thermo Fisher
436 Scientific). When adherent and lymphoma B cells were co-encapsulated, a
437 suspension of 2×10^6 cells of each cell type were used. 200µL of the cell suspension
438 is injected into a cooling part to maintain Matrigel liquid (Alessandri et al., 2016). The
439 flow rates are set to 45mL/h, 45mL/h and 30mL/h for the alginate, sorbitol and cell
440 suspension, respectively. The device is positioned 40-50 cm above a petri dish
441 containing 100mM $CaCl_2$ solution for capsule gelling and collection. To improve
442 capsule shape and monodispersity an alginate charging part and copper ring (21mm
443 OD, RadioSpares), both connected to a high voltage (2 kV) generator (Stanford
444 Research PS350, Acal BFI, France) are introduced, as described in (Trushko et al.,
445 2020). The charged formed droplets passing through the copper ring under electrical
446 tension get deflected as they cross the ring, creating a splay-like jet that prevents
447 capsule coalescence. Once formed inside the calcium bath, capsules are washed
448 with DMEM and transferred to cell culture medium.

449

450 **Cell lines, suspension, monolayer and encapsulated cell culture**

451 Stromal cells (TSC) were isolated as previously described (Ame-Thomas et
452 al., 2007; Guilloton et al., 2012) from human tonsils collected from children
453 undergoing routine tonsillectomy, considered as chirurgical wastes. GFP-expressing
454 TSC cells were established after transduction with lentivirus carrying the pUltra (gift
455 from Malcolm Moore (Addgene plasmid # 24129; http://n2t.net/addgene:24129;
456 RRID: Addgene_24129), which contained the enhanced GFP gene under the control
457 of Ubc promoter and produced as previously described (WU and LU, 2007). TSC
458 were transduced in RPMI supplemented with 2% FBS containing pUltra concentrated

lentiviral supernatant with MOI of 4. On the next day, the medium was replaced with standard culture medium. After one week, $eGFP^{high}$ TSC were isolated using a cell sorter (FACS Aria, BD Biosciences). For all the experiments reported in the present work, TSC were used from P9 to P13. DLBCL SU-DHL-4 and FL DOHH2 cell lines were obtained from the DSMZ cell collection (Braunschweig, Germany). HLY-1 cell line was kindly provided by Dr F. Meggetto (CRCT, Toulouse, France). Cells were routinely cultured in RPMI medium (Thermo Fisher Scientific), supplemented with 10% FBS (Dutscher, Brumath, France) under humid atmosphere containing 5% CO_2, with medium changed 3 times a week. One day prior to encapsulation, cells were cultured in DMEM supplemented with 10% FBS. Once cellular capsules were formed following the protocol described above, they were cultured in 75 cm^2 flasks in DMEM supplemented with 10% FBS under humid atmosphere containing 5% CO_2, with medium changed 2 times a week. Depending on the type of experiments, capsules were sampled and transferred to dedicated culture supports, e.g. for imaging, or treated in bulk conditions and subsequently analyzed, e.g. for FACS.

Spheroid growth measurement

At various post-encapsulation culture times, we selected about 200 capsules. Capsules were dissolved by incubation in PBS containing 1 mM EGTA and the spheroids were mechanically dissociated by pipetting. When spheroids were too cohesive, trypsin-EDTA was added to improve cell dissociation. The cell suspension was centrifuged and re-suspended in 200 µL of PBS and 50 µL of Precision Count Beads (BioLegend, Ozyme). The number of cells was then determined in a given cell suspension volume of 100 µL using flow cytometry (FACS Calibur, BD biosciences) according to the manufacturer's instructions. To evaluate the cell death in spheroids,

propidium iodide (PI) (10 µg/mL) was added to the cell suspension and PI fluorescence was analyzed by flow cytometry using Cell Quest or FlowJo (BD biosciences).

Immunofluorescence staining of spheroids

In capsule staining

Capsules were fixed in DMEM w/o phenol red (Pan Biotech, Dutscher), containing 4% paraformaldehyde for 20 min at room temperature (RT). After rinsing, capsules were incubated for 30 min in DMEM w/o phenol red/ 0.1% triton X-100. Following a step of saturation with a solution containing DMEM w/o phenol red/ BSA 1% /FBS 2% for 1h at RT, capsules were incubated with primary antibody overnight at 4°C under shaking. Primary antibody was revealed by incubation of capsules with secondary Alexa-coupled antibody for 2h at RT. Nuclei were stained by incubation of capsules with Hoechst 33258 for 30 min at RT. To determine the role of Matrigel in the stromal network establishment, immunofluorescence using a rabbit anti-human pan laminin antibody revealed by goat anti rabbit Alexa 633 secondary antibody, was performed to visualize Matrigel, stromal cells were GFP positive and nuclei was stained with Hoechst 33258. Z-stacks were acquired using a Zeiss LSM 510 meta confocal microscope with a 25x objective (N.A 0.7). 3D rendering was obtained using UCSF Chimera software (RBVI, San Francisco, USA).

FFPE staining

To analyze protein expression inside spheroids, immunofluorescence on FFPE (Formalin-Fixed Paraffin-Embedded) spheroids sections (3-5 µm thick) were performed. Alginate shells were dissolved and spheroids were fixed as described

above. Spheroids were then pre-embedded in 2% agarose and further embedded in a paraffin block. Immunofluorescence staining was then performed as previously described (Andrique et al., 2019). Images were acquired using a Zeiss LSM 510 meta confocal microscope (Zeiss, Göttingen, Germany) with a 25x objective (N.A 0.7). Then images obtained were processed using Fiji.

3D cell morphology quantification

Capsules were fixed at various post-encapsulation culture times and each capsule was placed in an agarose well of the Universlide microscopy chamber (Alessandri et al., 2017), which allowed immobilization of the capsules as required for stable z-stack acquisition and medium throughput 3D imaging. Cell nuclei were stained with Hoechst 33258 and stromal cells were visualized by the GFP expression. Images were acquired using a Leica SP8 confocal microsocpe with a 20X dry objective (NA 0.7). To measure the evolution of TSC complexity over time two parameters were measured: the sphericity defined as $\sqrt[3]{\frac{36\times\pi\times\text{Volume of particle}^2}{\text{Surface of particle}^3}}$ and the branchness defined as $\frac{Volume\ of\ particule\ convex\ hull}{Volume\ of\ particule}$. To obtain these values, we applied a locally adjusted threshold to the green signal, performed 3D segmentation (3D suite plugin, Fiji (Ollion et al., 2013). For the two parameters, the values of all “particles” contained in one capsule were averaged. Thus, each capsule was characterized by one mean value for sphericity and branchness. 10-18 capsules were analyzed per time point

Multiplex fluorescence microscopy

Patients were recruited under institutional review board approval following informed consent process according to the declaration of Helsinki and the French National Cancer Institute ethic committee recommendations. Tissue samples included tonsils collected from routine tonsillectomy, and lymph nodes obtained from grade 1-2 FL and from DLBCL patients.

Four-micrometer-thick whole-slide sections, obtained with a microtome (Histocore multicut Leicabiosystems, Nanterre, France) from FFPE tissue or spheroids blocks, were transferred onto plus-charged slides (VWR international), followed by multiplex immunofluorescence staining with a U DISCOVERY 5 plex immunofluorescence (Roche Diagnostics, Meylan, France). Three sequential rounds of staining were performed each including heat deactivation step, followed by incubation with primary antibody and corresponding HRP secondary antibody. Hence, rat anti-podoplanin (Thermo Fisher Scientific NZ-1.3), mouse Anti-PAX5 antibody (Abcam ab224660), and sheep anti-transglutaminase (R&D AF4376) expressions were visualized on the same section using HRP enzyme mediated deposition of the tyramide coupled to rhodamine, DCC and FAM fluorophores (kits Ventana Medical Systems, Tucson, Ariz), respectively, that covalently binds to the tissue at the site of the reaction. After 3 sequential reactions, sections were counterstained with DAPI and coverslipped using fluoromount (Enzo Life Sciences, Farmingdale, NY, USA). Visualization was performed with the Nanozoomer (Hamamatsu Photonics, Massy, France) equipped with the multicolor fluorescence module.

Cell co-culture and cell sorting:

2D co-cultures were performed over 3 days. 3×10^5DOHH2 (1.5×10^5/mL) were plated on 5×10^4 TSC /cm^2 in 6 well plates. For cell sorting, cells were trypsinized (Thermo Fisher Scientific) for 12 min at 37 °C and washed with medium DMEM 10% FBS. 3D co-cultures were performed over 10 days. For cell sorting, after dissolution of the alginate shells, cells were rinsed with DMEM 10% FBS and centrifuged for 7 min at 1700 rpm, incubated with trypsin at 37 °C for 15 min, and rinsed with medium DMEM 10% FBS. Cells were stained for 20 min on ice with mouse anti-human CD20 APC-H7 and mouse anti-human CD73 PE. After DAPI staining, cell sorting was processed by the FACSAria II (BD Biosciences).

RT q-PCR arrays

After cell sorting, RNA extraction from DOHH2 co-cultured in 2D or 3D with TSC cells was done using Nucleospin RNA XS Micro kit (PN 740990) from Macherey Nagel (Hoerdt, France). cDNA were synthesized using reverse transcription master mix (Fluidigm, USA, PN 100-6297), followed by gene expression preamplification with Fluidigm Preamp Master mix (PN 100-5744) and Taq Man assays and followed by RT-QPCR. Assay-on-demand primers, probes, and TaqMan gene expression Master Mix were obtained from Thermo Fisher Scientific. Gene expression was measured using 96.96 Dynamic Array™ IFCs and the BioMark™ HD System from Fluidigm, based on ΔCt calculation method. A tonsil pool was used as appropriate DOHH2 expression external control. For each sample, the Ct value for the gene of interest was determined and normalized to its respective mean value of housekeeping genes (*ABL1* and *GAPDH*). Data were represented through a heatmap using the pheatmap R package. In addition, differentially expressed genes

were analyzed in Affymetrix data sets comparing purified FL B cells and purified centrocytes (GSE85233 and GSE136249) (Pangault et al., 2020).

Chemotherapeutic toxicity measurement

To compare the drug toxicities between lymphoma cells cultured in suspension and in spheroids, 0.5×10^6cells/well co-cultured or not with 5×10^4 TSC /cm^2 or 100 confluent spheroids were distributed in 6-well plates and treated or not with doxorubicin for 24h. Then, cell death was assessed by flow cytometry after Annexin V-APC labelling according to the manufacturer's instructions.

Statistical analyses

All data were expressed as means ± SEM. The significance of differences was calculated using the parametric ANOVA or the non-parametric U-Mann and Whitney or Wilcoxon tests, as appropriate. (*P<0.05, **P<0.01, ***P<0.001, ****P<0.0001). Statistical analyses were performed using GraphPad Prism 8 software.

FUNDINGS

This work was supported by INSERM, University of Bordeaux, Ligue Régionale contre le Cancer (comités de Gironde, Charentes, Pyrénées, Landes), the Fondation ARC pour la Recherche sur le Cancer (Grant PGA1 RF20170205386), Emergence GSO Cancéropole, and SIRIC BRIO. SL is supported by Ligue Nationale contre le Cancer and C.L. is a recipient of a doctoral fellowship from the FHU CAMIn and LBB (Léa Broca-Brisson) of a master fellowship from CNRS GDR Imabio.

ACKNOWLEDGMENTS

We thank Stéphanie Durand-Panteix for her technical support with transduction experiments. We thank Atika Zouine and Vincent Pitard for technical assistance at the Flow cytometry facility, CNRS UMS 3427, INSERM US 005, Univ. Bordeaux, F-33000 Bordeaux, France. We acknowledge the Bordeaux Imaging Center, a service unit of the CNRS-INSERM and Bordeaux University, member of the national infrastructure France BioImaging supported by the French Research Agency (ANR-10-INBS-04). A part of immunofluorescence study was performed on the Microscopy Rennes Imaging Center (MRic-ALMF; UMS 6480 Biosit, Rennes, France) member of the national infrastructure France-BioImaging. Cell sorting was performed at the Biosit Flow Cytometry and Cell Sorting Facility CytomeTRI (UMS 6480 Biosit, Rennes, France).

REFERENCES

Alessandri, K., Andrique, L., Feyeux, M., Bikfalvi, A., Nassoy, P., Recher, G., 2017. All-in-one 3D printed microscopy chamber for multidimensional imaging, the UniverSlide. Sci.Rep. 7, 42378. https://doi.org/10.1038/srep42378

Alessandri, K., Feyeux, M., Gurchenkov, B., Delgado, C., Trushko, A., Krause, K.H., Vignjevic, D., Nassoy, P., Roux, A., 2016. A 3D printed microfluidic device for production of functionalized hydrogel microcapsules for culture and differentiation of human Neuronal Stem Cells (hNSC). Lab Chip. 16, 1593–1604. https://doi.org/10.1039/c6lc00133e

Alessandri, K., Sarangi, B.R., Gurchenkov, V.V., Sinha, B., Kiessling, T.R., Fetler, L., Rico, F., Scheuring, S., Lamaze, C., Simon, A., Geraldo, S., Vignjevic, D., Domejean, H., Rolland, L., Funfak, A., Bibette, J., Bremond, N., Nassoy, P., 2013. Cellular capsules as a tool for multicellular spheroid production and for investigating the mechanics of tumor progression in vitro. Proc.Natl.Acad.Sci.U.S.A 110, 14843–14848. https://doi.org/10.1073/pnas.1309482110

Alizadeh, A.A., Eisen, M.B., Davis, R.E., Ma, C., Lossos, I.S., Rosenwald, A., Boldrick, J.C., Sabet, H., Tran, T., Yu, X., Powell, J.I., Yang, L., Marti, G.E., Moore, T., Hudson, J., Lu, L., Lewis, D.B., Tibshirani, R., Sherlock, G., Chan, W.C., Greiner, T.C., Weisenburger, D.D., Armitage, J.O., Warnke, R., Levy, R., Wilson, W., Grever, M.R., Byrd, J.C., Botstein, D., Brown, P.O., Staudt, L.M., 2000. Distinct types of diffuse large B-cell lymphoma identified by gene expression profiling. Nature 403, 503–511. https://doi.org/10.1038/35000501

Ame-Thomas, P., Maby-El, H.H., Monvoisin, C., Jean, R., Monnier, D., Caulet-Maugendre, S., Guillaudeux, T., Lamy, T., Fest, T., Tarte, K., 2007. Human

643 mesenchymal stem cells isolated from bone marrow and lymphoid organs support
644 tumor B-cell growth: role of stromal cells in follicular lymphoma pathogenesis.
645 Blood 109, 693–702. https://doi.org/10.1182/blood-2006-05-020800
646 Andrique, L., Recher, G., Alessandri, K., Pujol, N., Feyeux, M., Bon, P., Cognet, L.,
647 Nassoy, P., Bikfalvi, A., 2019. A model of guided cell self-organization for rapid
648 and spontaneous formation of functional vessels. Science Advances 5.
649 https://doi.org/10.1126/sciadv.aau6562
650 Apoorva, F., Loiben, A.M., Shah, S.B., Purwada, A., Fontan, L., Goldstein, R., Kirby,
651 B.J., Melnick, A.M., Cosgrove, B.D., Singh, A., 2018. How Biophysical Forces
652 Regulate Human B Cell Lymphomas. Cell Reports 23, 499–511.
653 https://doi.org/10.1016/j.celrep.2018.03.069
654 Astarita, J.L., Cremasco, V., Fu, J., Darnell, M.C., Peck, J.R., Nieves-Bonilla, J.M.,
655 Song, K., Kondo, Y., Woodruff, M.C., Gogineni, A., Onder, L., Ludewig, B.,
656 Weimer, R.M., Carroll, M.C., Mooney, D.J., Xia, L., Turley, S.J., 2015. The CLEC-
657 2–podoplanin axis controls the contractility of fibroblastic reticular cells and lymph
658 node microarchitecture. Nature Immunology 16, 75–84.
659 https://doi.org/10.1038/ni.3035
660 Barreca, A., Martinengo, C., Annaratone, L., Righi, L., Chiappella, A., Ladetto, M.,
661 Demurtas, A., Chiusa, L., Stacchini, A., Crosetto, N., van Oudenaarden, A.,
662 Chiarle, R., 2014. Inter- and intratumoral heterogeneity of BCL2 correlates with
663 IgH expression and prognosis in follicular lymphoma. Blood Cancer Journal 4,
664 e249–e249. https://doi.org/10.1038/bcj.2014.67
665 Benien, P., Swami, A., 2014. 3D tumor models: history, advances and future
666 perspectives. Future Oncol 10, 1311–1327. https://doi.org/10.2217/fon.13.274

667 Bissell, M.J., Radisky, D., 2001. Putting tumours in context. Nat.Rev.Cancer 1, 46–
668 54. https://doi.org/10.1038/35094059
669 Chen, J., Alexander, J.S., Orr, A.W., 2012. Integrins and Their Extracellular Matrix
670 Ligands in Lymphangiogenesis and Lymph Node Metastasis. Int J Cell Biol 2012.
671 https://doi.org/10.1155/2012/853703
672 Coplen, D.E., Macarak, E.J., Howard, P.S., 2003. Matrix synthesis by bladder smooth
673 muscle cells is modulated by stretch frequency. In Vitro Cell.Dev.Biol.-Animal 39,
674 157–162. https://doi.org/10.1007/s11626-003-0010-3
675 Däster, S., Amatruda, N., Calabrese, D., Ivanek, R., Turrini, E., Droeser, R.A., Zajac,
676 P., Fimognari, C., Spagnoli, G.C., Iezzi, G., Mele, V., Muraro, M.G., 2016.
677 Induction of hypoxia and necrosis in multicellular tumor spheroids is associated
678 with resistance to chemotherapy treatment. Oncotarget 8, 1725–1736.
679 https://doi.org/10.18632/oncotarget.13857
680 Decaup, E., Jean, C., Laurent, C., Gravelle, P., Fruchon, S., Capilla, F., Marrot, A., Al
681 Saati, T., Frenois, F.-X., Laurent, G., Klein, C., Varoqueaux, N., Savina, A.,
682 Fournié, J.-J., Bezombes, C., 2013. Anti-tumor activity of obinutuzumab and
683 rituximab in a follicular lymphoma 3D model. Blood Cancer J 3, e131.
684 https://doi.org/10.1038/bcj.2013.32
685 Decaup, E., Rossi, C., Gravelle, P., Laurent, C., Bordenave, J., Tosolini, M., Tourette,
686 A., Perrial, E., Dumontet, C., Poupot, M., Klein, C., Savina, A., Fournié, J.-J.,
687 Bezombes, C., 2019. A Tridimensional Model for NK Cell-Mediated ADCC of
688 Follicular Lymphoma. Front. Immunol. 10.
689 https://doi.org/10.3389/fimmu.2019.01943
690 Della-Torre, E., Rigamonti, E., Perugino, C., Baghai-Sain, S., Sun, N., Kaneko, N.,
691 Maehara, T., Rovati, L., Ponzoni, M., Milani, R., Lanzillotta, M., Mahajan, V.,

692 Mattoo, H., Molineris, I., Deshpande, V., Stone, J.H., Falconi, M., Manfredi, A.A.,
693 Pillai, S., 2020. B lymphocytes directly contribute to tissue fibrosis in patients with
694 IgG4-related disease. Journal of Allergy and Clinical Immunology 145, 968-
695 981.e14. https://doi.org/10.1016/j.jaci.2019.07.004
696 Desoize, B., 2000. Multicellular resistance: a paradigm for clinical resistance? Critical
697 Reviews in Oncology/Hematology 36, 193–207. https://doi.org/10.1016/S1040-
698 8428(00)00086-X
699 Doméjean, H., Pierre, M. de la M.S., Funfak, A., Atrux-Tallau, N., Alessandri, K.,
700 Nassoy, P., Bibette, J., Bremond, N., 2016. Controlled production of sub-millimeter
701 liquid core hydrogel capsules for parallelized 3D cell culture. Lab Chip 17, 110–
702 119. https://doi.org/10.1039/C6LC00848H
703 Fletcher, A.L., Acton, S.E., Knoblich, K., 2015. Lymph node fibroblastic reticular cells
704 in health and disease. Nat. Rev. Immunol. 15, 350–361.
705 https://doi.org/10.1038/nri3846
706 Fowler, N.H., Cheah, C.Y., Gascoyne, R.D., Gribben, J., Neelapu, S.S., Ghia, P.,
707 Bollard, C., Ansell, S., Curran, M., Wilson, W.H., O'Brien, S., Grant, C., Little, R.,
708 Zenz, T., Nastoupil, L.J., Dunleavy, K., 2016. Role of the tumor microenvironment
709 in mature B-cell lymphoid malignancies. Haematologica 101, 531–540.
710 https://doi.org/10.3324/haematol.2015.139493
711 Gallouet, A.S., Travert, M., Bresson-Bepoldin, L., Guilloton, F., Pangault, C., Caulet-
712 Maugendre, S., Lamy, T., Tarte, K., Guillaudeux, T., 2014. COX-2-independent
713 effects of celecoxib sensitize lymphoma B cells to TRAIL-mediated apoptosis.
714 Clin.Cancer Res. 20, 2663–2673. https://doi.org/10.1158/1078-0432.CCR-13-2305

715 Goda, N., Dozier, S.J., Johnson, R.S., 2003. HIF-1 in Cell Cycle Regulation,
716 Apoptosis, and Tumor Progression. Antioxidants & Redox Signaling 5, 467–473.
717 https://doi.org/10.1089/152308603768295212
718 Gravelle, P., Jean, C., Familiades, J., Decaup, E., Blanc, A., Bezombes-Cagnac, C.,
719 Laurent, C., Savina, A., Fournié, J.-J., Laurent, G., 2014. Cell growth in
720 aggregates determines gene expression, proliferation, survival, chemoresistance,
721 and sensitivity to immune effectors in follicular lymphoma. Am. J. Pathol. 184,
722 282–295. https://doi.org/10.1016/j.ajpath.2013.09.018
723 Guilloton, F., Caron, G., Menard, C., Pangault, C., Ame-Thomas, P., Dulong, J., De,
724 V.J., Rossille, D., Henry, C., Lamy, T., Fouquet, O., Fest, T., Tarte, K., 2012.
725 Mesenchymal stromal cells orchestrate follicular lymphoma cell niche through the
726 CCL2-dependent recruitment and polarization of monocytes. Blood 119, 2556–
727 2567. https://doi.org/10.1182/blood-2011-08-370908
728 He, Y., Macarak, E.J., Korostoff, J.M., Howard, P.S., 2004. Compression and
729 Tension: Differential Effects on Matrix Accumulation by Periodontal Ligament
730 Fibroblasts In Vitro. Connective Tissue Research 45, 28–39.
731 https://doi.org/10.1080/03008200490278124
732 Heckman, C.A., Mehew, J.W., Boxer, L.M., 2002. NF-kappaB activates Bcl-2
733 expression in t(14;18) lymphoma cells. Oncogene 21, 3898–3908.
734 https://doi.org/10.1038/sj.onc.1205483
735 Heldt, F.S., Barr, A.R., Cooper, S., Bakal, C., Novák, B., 2018. A comprehensive
736 model for the proliferation–quiescence decision in response to endogenous DNA
737 damage in human cells. PNAS 115, 2532–2537.
738 https://doi.org/10.1073/pnas.1715345115

739 Hu, K.H., Butte, M.J., 2016. T cell activation requires force generation. The Journal of
740 cell biology 213, 535–542. https://doi.org/10.1083/jcb.201511053
741 Huet, S., Sujobert, P., Salles, G., 2018. From genetics to the clinic: a translational
742 perspective on follicular lymphoma. Nat Rev Cancer 18, 224–239.
743 https://doi.org/10.1038/nrc.2017.127
744 Hwang, I.-Y., Hwang, K.-S., Park, C., Harrison, K.A., Kehrl, J.H., 2013. Rgs13
745 Constrains Early B Cell Responses and Limits Germinal Center Sizes. PLoS ONE
746 8, e60139. https://doi.org/10.1371/journal.pone.0060139
747 Kennedy, R., Klein, U., 2018. Aberrant Activation of NF-κB Signalling in Aggressive
748 Lymphoid Malignancies. Cells 7, 189. https://doi.org/10.3390/cells7110189
749 Koshiji, M., Kageyama, Y., Pete, E.A., Horikawa, I., Barrett, J.C., Huang, L.E., 2004.
750 HIF-1α induces cell cycle arrest by functionally counteracting Myc. EMBO J 23,
751 1949–1956. https://doi.org/10.1038/sj.emboj.7600196
752 Meng, K.P., Majedi, F.S., Thauland, T.J., Butte, M.J., 2020. Mechanosensing through
753 YAP controls T cell activation and metabolism. Journal of Experimental Medicine
754 217, e20200053. https://doi.org/10.1084/jem.20200053
755 Mikaelsson, E., Danesh-Manesh, A.H., Lüppert, A., Jeddi-Tehrani, M., Rezvany, M.-
756 R., Sharifian, R.A., Safaie, R., Roohi, A., Osterborg, A., Shokri, F., Mellstedt, H.,
757 Rabbani, H., 2005. Fibromodulin, an extracellular matrix protein: characterization
758 of its unique gene and protein expression in B-cell chronic lymphocytic leukemia
759 and mantle cell lymphoma. Blood 105, 4828–4835. https://doi.org/10.1182/blood-
760 2004-10-3941
761 Ollion, J., Cochennec, J., Loll, F., Escudé, C., Boudier, T., 2013. TANGO: a generic
762 tool for high-throughput 3D image analysis for studying nuclear organization.
763 Bioinformatics 29, 1840–1841. https://doi.org/10.1093/bioinformatics/btt276

764 Pandey, S., Mourcin, F., Marchand, T., Nayar, S., Guirriec, M., Pangault, C.,
765 Monvoisin, C., Amé-Thomas, P., Guilloton, F., Dulong, J., Coles, M., Fest, T.,
766 Mottok, A., Barone, F., Tarte, K., 2017. IL-4/CXCL12 loop is a key regulator of
767 lymphoid stroma function in follicular lymphoma. Blood 129, 2507–2518.
768 https://doi.org/10.1182/blood-2016-08-737239
769 Pangault, C., Amé-Thomas, P., Rossille, D., Dulong, J., Caron, G., Nonn, C.,
770 Chatonnet, F., Desmots, F., Launay, V., Lamy, T., Fest, T., Tarte, K., 2020.
771 Integrative Analysis of Cell Crosstalk within Follicular Lymphoma Cell Niche:
772 Towards a Definition of the FL Supportive Synapse. Cancers 12, 2865.
773 https://doi.org/10.3390/cancers12102865
774 Perret, E., Leung, A., Morel, A., Feracci, H., Nassoy, P., 2002. Versatile Decoration
775 of Glass Surfaces To Probe Individual Protein−Protein Interactions and Cellular
776 Adhesion. Langmuir 18, 846–854. https://doi.org/10.1021/la015601y
777 Purwada, A., Jaiswal, M.K., Ahn, H., Nojima, T., Kitamura, D., Gaharwar, A.K.,
778 Cerchietti, L., Singh, A., 2015. Ex vivo engineered immune organoids for
779 controlled germinal center reactions. Biomaterials 63, 24–34.
780 https://doi.org/10.1016/j.biomaterials.2015.06.002
781 Ramezani-Rad, P., Rickert, R.C., 2017. Murine models of germinal center derived-
782 lymphomas. Current Opinion in Immunology, Lymphocyte development and
783 activation * Tumour immunology 45, 31–36.
784 https://doi.org/10.1016/j.coi.2016.12.002
785 Sabhachandani, P., Sarkar, S., Mckenney, S., Ravi, D., Evens, A.M., Konry, T., 2019.
786 Microfluidic assembly of hydrogel-based immunogenic tumor spheroids for
787 evaluation of anticancer therapies and biomarker release. Journal of Controlled
788 Release 295, 21–30. https://doi.org/10.1016/j.jconrel.2018.12.010

789 Scott, D.W., Gascoyne, R.D., 2014. The tumour microenvironment in B cell
790 lymphomas. Nature Reviews Cancer 14, 517–534. https://doi.org/10.1038/nrc3774
791 Sehn, L.H., Gascoyne, R.D., 2015. Diffuse large B-cell lymphoma: optimizing
792 outcome in the context of clinical and biologic heterogeneity. Blood 125, 22–32.
793 https://doi.org/10.1182/blood-2014-05-577189
794 Sgambato, A., Cittadini, A., Faraglia, B., Weinstein, I.B., 2000. Multiple functions of
795 p27Kip1 and its alterations in tumor cells: a review. Journal of Cellular Physiology
796 183, 18–27. https://doi.org/10.1002/(SICI)1097-4652(200004)183:1<18::AID-
797 JCP3>3.0.CO;2-S
798 Shi, G.-X., Harrison, K., Wilson, G.L., Moratz, C., Kehrl, J.H., 2002. RGS13
799 Regulates Germinal Center B Lymphocytes Responsiveness to CXC Chemokine
800 Ligand (CXCL)12 and CXCL13. J Immunol 169, 2507–2515.
801 https://doi.org/10.4049/jimmunol.169.5.2507
802 Smith, A., Howell, D., Patmore, R., Jack, A., Roman, E., 2011. Incidence of
803 haematological malignancy by sub-type: a report from the Haematological
804 Malignancy Research Network. British Journal of Cancer 105, 1684–1692.
805 https://doi.org/10.1038/bjc.2011.450
806 Sobocinski, G.P., Toy, K., Bobrowski, W.F., Shaw, S., Anderson, A.O., Kaldjian, E.P.,
807 2010. Ultrastructural localization of extracellular matrix proteins of the lymph node
808 cortex: evidence supporting the reticular network as a pathway for lymphocyte
809 migration. BMC Immunol 11, 42. https://doi.org/10.1186/1471-2172-11-42
810 Sutherland, R.M., 1988. Cell and environment interactions in tumor microregions: the
811 multicell spheroid model. Science 240, 177–184.
812 https://doi.org/10.1126/science.2451290

Tancred, T.M., Belch, A.R., Reiman, T., Pilarski, L.M., Kirshner, J., 2009. Altered Expression of Fibronectin and Collagens I and IV in Multiple Myeloma and Monoclonal Gammopathy of Undetermined Significance. J Histochem Cytochem 57, 239–247. https://doi.org/10.1369/jhc.2008.952200

Tellier, J., Menard, C., Roulland, S., Martin, N., Monvoisin, C., Chasson, L., Nadel, B., Gaulard, P., Schiff, C., Tarte, K., 2014. Human t(14;18)positive germinal center B cells: a new step in follicular lymphoma pathogenesis? Blood 123, 3462–3465. https://doi.org/10.1182/blood-2013-12-545954

Teras, L.R., DeSantis, C.E., Cerhan, J.R., Morton, L.M., Jemal, A., Flowers, C.R., 2016. 2016 US lymphoid malignancy statistics by World Health Organization subtypes. CA: A Cancer Journal for Clinicians 66, 443–459. https://doi.org/10.3322/caac.21357

Tian, Y.F., Ahn, H., Schneider, R.S., Yang, S.N., Roman-Gonzalez, L., Melnick, A.M., Cerchietti, L., Singh, A., 2015. Integrin-specific hydrogels as adaptable tumor organoids for malignant B and T cells. Biomaterials 73, 110–119. https://doi.org/10.1016/j.biomaterials.2015.09.007

Trushko, A., Di Meglio, I., Merzouki, A., Blanch-Mercader, C., Abuhattum, S., Guck, J., Alessandri, K., Nassoy, P., Kruse, K., Chopard, B., Roux, A., 2020. Buckling of an Epithelium Growing under Spherical Confinement. Developmental Cell 54, 655-668.e6. https://doi.org/10.1016/j.devcel.2020.07.019

Verdière, L., Mourcin, F., Tarte, K., 2018. Microenvironment signaling driving lymphomagenesis. Current Opinion in Hematology 25, 335. https://doi.org/10.1097/MOH.0000000000000440

836 Wu, C., Lu, Y., 2007. Inclusion of high molecular weight dextran in calcium
837 phosphate-mediated transfection significantly improves gene transfer efficiency.
838 Cell Mol Biol (Noisy-le-grand) 53, 67–74.
839 Zhang, Jun, Seet, C.S., Sun, C., Li, J., You, D., Volk, A., Breslin, P., Li, X., Wei, W.,
840 Qian, Z., Zeleznik-Le, N.J., Zhang, Z., Zhang, Jiwang, 2013. p27kip1 maintains a
841 subset of leukemia stem cells in the quiescent state in murine MLL-leukemia. Mol
842 Oncol 7, 1069–1082. https://doi.org/10.1016/j.molonc.2013.07.011
843 Zinkel, S., Gross, A., Yang, E., 2006. BCL2 family in DNA damage and cell cycle
844 control. Cell Death Differ. 13, 1351–1359. https://doi.org/10.1038/sj.cdd.4401987
845

FIGURE LEGENDS

Figure 1: B NHL spheroids obtained by using the cellular capsule technology.

A: Representative images of cell growth in alginate capsule shells over time for the various cell lines. Scale bar: 100µm. **B:** Percentage of SU-DHL-4 and HLY1 cell death measured after shell dissolution and cell dissociation at various culture time points. To evaluate the cell death propidium iodide (PI) (10µg/mL) was added to the cell suspension and PI fluorescence was analyzed by flow cytometry (n=3). **C**: Immunostaining showing the repartition of proliferating and apoptotic cells in SU-DHL-4 and HLY1-derived spheroids at day 8 or 12 post-encapsulation. Five micrometers thick sections were stained with anti-Ki67 (Ki67, in green), and anti-cleaved caspase 3 (CC3, in red), to identify proliferating and dead cells, respectively. Nuclei are depicted in blue. Scale bar: 100µm.

Figure 2: B NHL spheroids are cohesive and express extracellular matrix.

A: Pictures showing the maintenance of SU-DHL-4 spheroids after the capsule dissolution by incubation in PBS containing 1 mM EGTA. Scale bar: 100µm. **B:** Immunostaining showing the expression of extracellular matrix in cells cultured in suspension (2D) or in spheroids (3D). After fixation, cell suspension was centrifuged and pellet was embedded in 2% agarose and then in paraffin, as performed for spheroids. Extracellular matrix components were visualized by staining with anti-pan laminin, anti- fibronectin and anti- collagen I antibodies on 5µm thick sections. Nuclei are depicted in blue. Scale bar: 50µm.

Figure 3: The establishment of a stromal network is necessary to reproduce stromal-dependent B NHL cell growth.

A: Effect of Matrigel (Mg) and TSC on spheroid growth. Left panel, representative images of spheroids obtained from B cells encapsulated with or without Mg and TSC at D7 (HLY1), D6 (SU-DHL-4) or D10 (DOHH2) of culture. Scale bar: 200µm. Right panel, the cell number was evaluated at various culture time points in the different conditions (n=3). **B**: TSC network needs Mg to be established. *Left*, example of TSC encapsulated without Mg. *Right*, example of TSC encapsulated with Mg. TSC were visualized in green by stable expression of GFP and nuclei were stained in blue with Hoechst 33252. Capsules were imaged 3 days after encapsulation. Images were maximum intensity projection from z-stacks. Scale bar: 100µm. **C:** TSC network is necessary to induce DOHH2 spheroid growth. DOHH2 were co-encapsulated with TSC with or without Mg for 10 days. TSC were visualized in green by stable expression of GFP. **D**: TSC/Mg interaction. TSC were encapsulated in the presence of Mg. After 3 days in culture, capsules were fixed and immunofluorescence was performed. Mg and TSC were visualized by staining with anti-human pan laminin (in red) and anti-GFP (in green), respectively. Nuclei were counterstained in blue with Hoechst 33258. Images were maximum intensity projection from z-stacks. Scale bar: 50µm. Yellow square is a crop showing the hanging of TSC on Mg coating. Scale bar: 10µm.

Figure 4: Self-organization of the stromal network.

A: Representatives images of capsules containing DOHH2 with Mg and TSC at different culture time point. After fixation, 10 to 18 spheroids for each time point were placed in an Universlide (Alessandri et al 2017). Images shown are Z-projection. TSC are shown in green and all the analyses were performed on green signal exclusively. Scale bar: 50µm (**B**) and (**C**) Sphericity and branchness indexes of green particles

contained in spheroids at different time after encapsulation, respectively. To determine significant differences, Anova was performed (*P<0.05, **P<0.01, ***P<0.001, ****P<0.0001). (**D**) Correlation of sphericity and branchness. For each time point, small dots represent individual spheroids whereas big dots represent the average values of all spheroids. Pearson correlation coefficient (R) was calculated using R software. The black line represents the regression line and the grey area represents the 95% confidence interval of the linear regression.

Figure 5: Spheroids recapitulate the FL stromal cell phenotype.

A: Tonsil B cells (revealed with anti-PAX5 antibody in blue) interact mainly with stromal cells expressing podoplanin (red). In FL lymph node, tumor B cells interact with stromal cells expressing podoplanin (red) and transglutaminase (green) markers. Scale bar: 250µm. In the 3D model TSCs adopt a particular phenotype in contact with DOHH2 by expressing transglutaminase (in green) and podoplanin (in red) markers. Scale bar: 100µm. **B**: 3D model at a higher magnification represents DOHH2 (in blue) in close contact with the podoplanin (shown by arrows in red) and transglutaminase (in green) expressing TSC network. Scale bars: 50µm. All images were stained with multiplex immunofluorescence microscopy method and visualized by Nanozoomer software.

Figure 6: Comparison of DOHH2 and FL B cell gene transcriptional expression profile.

A: Heatmap of DOHH2 gene expression levels evaluated by Real Time quantitative PCR (RT-qPCR) in cells cultured in 2D without (n=5) or with TSC (n=3), and in 3D with TSC (n=5). Analysis of DOHH2 transcriptional gene expression profiles, by RT-

921 qPCR, for **B**: *CDKN1A* and *CDKN1B*, **C**: *BCL2*, **D**: *EGLN1* and *VEGFA*, **F**: *RGS13*
922 and *CXCR4*, **G**: *RELB*, *TNFAIP3*, *BCL2A1* and *CFLAR*. DOHH2 were cultured in 2D
923 without (n=5) or with TSC (n=3) and in 3D with TSC (n=5) for 10 days. Variation gene
924 expression study between tonsil centrocytes (n=6) and FL lymph nodes tumoral B
925 cells (n=10) was studied by using Affymetrics micro-array analysis. A Kruskal Wallis
926 test was performed for *in vitro* experiments and a two tailed Mann Whitney test was
927 performed for the variation gene expression study between tonsil centrocytes (CC)
928 and LF lymph nodes tumoral B cells (FL C). ($p<0.05$*, $p<0,01$**). Bar represent the
929 geometric mean of independent experiments.
930
931 **Figure 7: Impact of 3D culture on drug response in B-NHL.**
932 **A-C:** Comparison of cell death induced by doxorubicin in SU-DHL-4 (**A**), HLY1 (**B**)
933 and DOHH2 (**C**) cultured in 2D or in 3D alone (*left panel*) or with TSC (2D+TSC or
934 3D+TSC) (*right panel*). For 2D culture, B cells were seeded alone or in presence of
935 TSC . For 3D culture, 100 confluent capsules, containing B cells alone or B cells with
936 TSC in presence of Matrigel, were seeded. 2D and 3D cultures were exposed to
937 doxorubicin at a concentration corresponding to its EC50and cell death was
938 evaluated after 24h.. **D:** Comparison of cell death induced by ABT-199 (1µM) in
939 DOHH2 cells cultured in 2D (*left panel*) or in 3D with TSC and Matrigel (*right panel*),
940 for 24h. The data represent mean ± SE of, at least, three independent experiments
941 (Wilcoxon test. *P<0.05, **P<0.01, ***P<0.001, ****P<0.0001).
942

Movie 1: Dissolution of alginate shell. Alginate shell of capsule containing SU-DHL-4 spheroid obtained after 10 days in culture is dissolved in a bath of PBS/EGTA. The images were acquired every 15 seconds until complete dissolution of capsule using an epifluorescence microscope (Leica DMI8).

Movie 2: Establishment of the stromal cell network. TSC expressing GFP and DOHH2 expressing dTomato were co-encapsulated in presence of Matrigel and placed in an Universlide in DMEM containing 10% FCS. The images were acquired immediately after encapsulation every 30 minutes for 12 hours using an epifluorescence microscope (Leica DMI8) equipped with a thermostatic and CO2 chamber (Live on Stage, Leica). Scale bar: 100µm.

Movie 3: Spatial organization of lymphoma spheroid. 3D reconstruction from optical sections using confocal microscopy of capsule containing DOHH2 with Mg and TSC cultured for 6 days.

Pathway	Gene
Cell survival	*CFLAR* *BCL2* *BRCA1* *BCL2A1*
Hypoxia	*VEGFA* *EGLN1*
B cell and BCR activation	*EBI3* *FYN* *CD79b* *CD79a* *RRM2*
Proliferation and differentiation	*CD24* *MET* *CD72*
Cell cycle	*CDC20* *CDK1* *CDK4*
Mechanosensitive	*PIEZO 1*
NFκB	*TNFAIP3* *BCL10* *RELB*
Quiescence	*CDKN1B* *CDKN1A*
Confinement and motility	*CXCR4* *RGS13* *P2RY8* *S1PR1* *CCR7* *GPR183* *CXCR5*
Apoptosis	*CASP8*
Cell and matrix interactions	*ADAM8*
Adhesion	*CD52*
Others	*RGS10* *KLF4* *LMO2* *IL6R*
Housekeeping genes	*GAPDH* *ABL1*

959 **Table 1: List of genes studied by RT-qPCR arrays.**

960

Figure 1

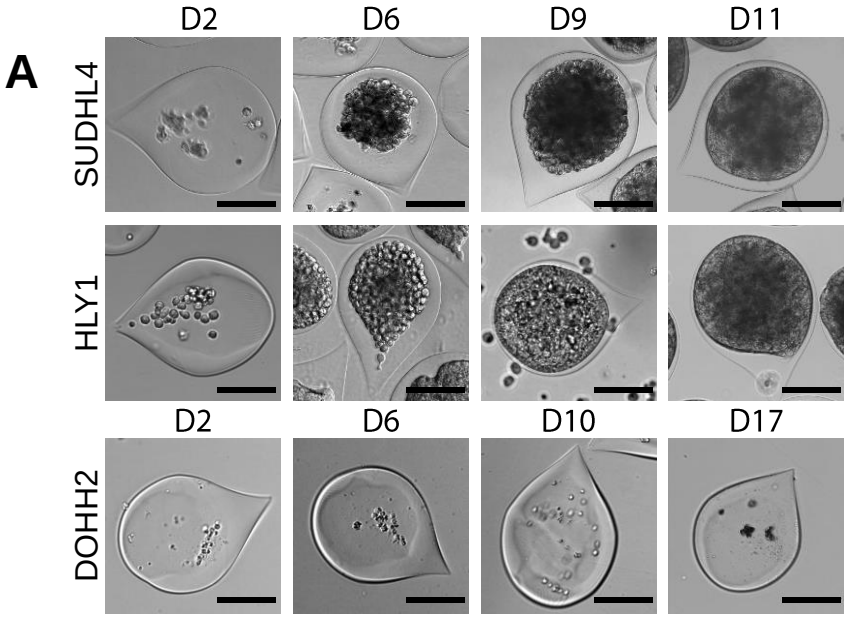
A
D2
D6
D9
D11
SUDHL4
HLY1
D2
D6
D10
D17
DOHH2

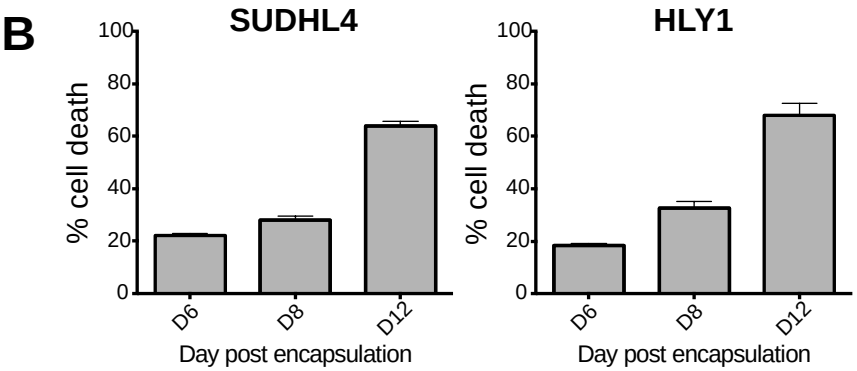
B
SUDHL4
HLY1
% cell death
100
80
60
40
20
0
D6
D8
D12
Day post encapsulation

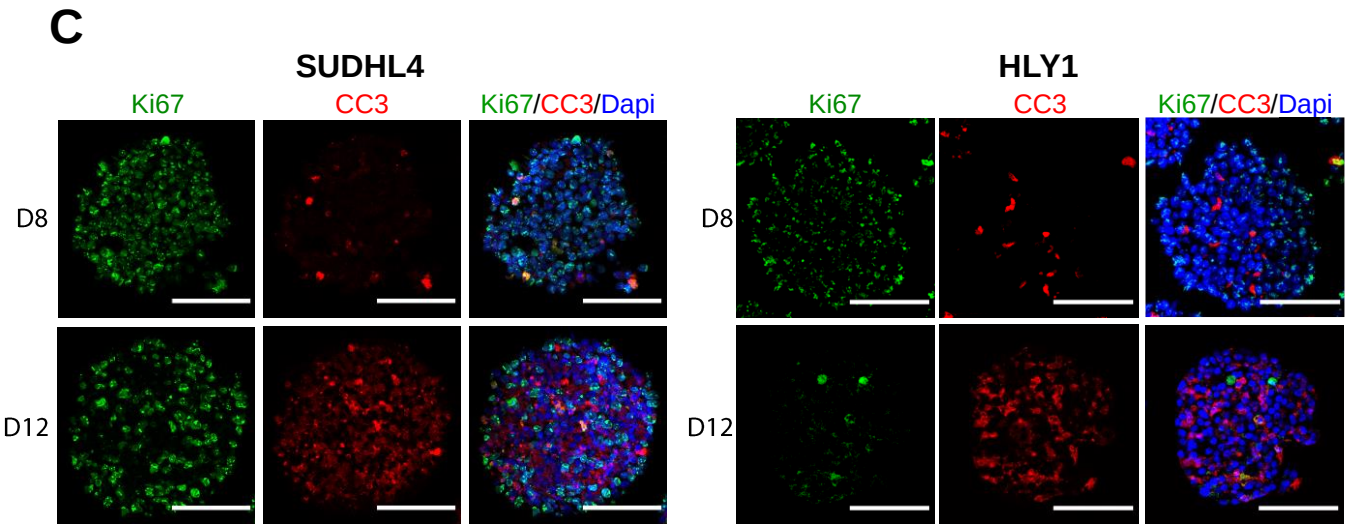
C
SUDHL4
HLY1
Ki67
CC3
Ki67/CC3/Dapi
D8
D12

Figure 2

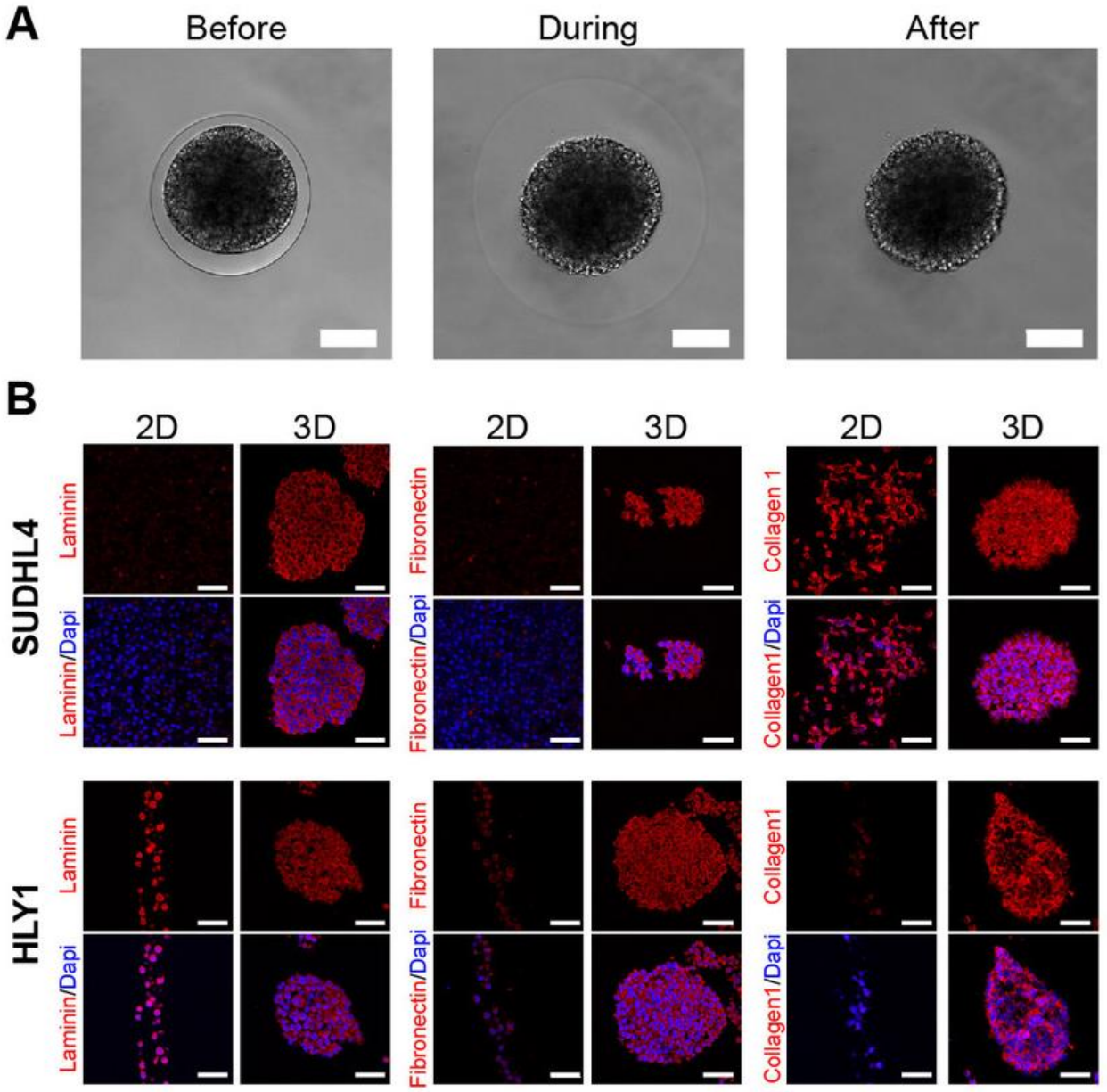
A
Before
During
After
B
2D
3D
2D
3D
2D
3D
SUDHL4
Laminin
Laminin/Dapi
Fibronectin
Fibronectin/Dapi
Collagen 1
Collagen1/Dapi
HLY1
Laminin
Laminin/Dapi
Fibronectin
Fibronectin/Dapi
Collagen1
Collagen1/Dapi

Figure 3

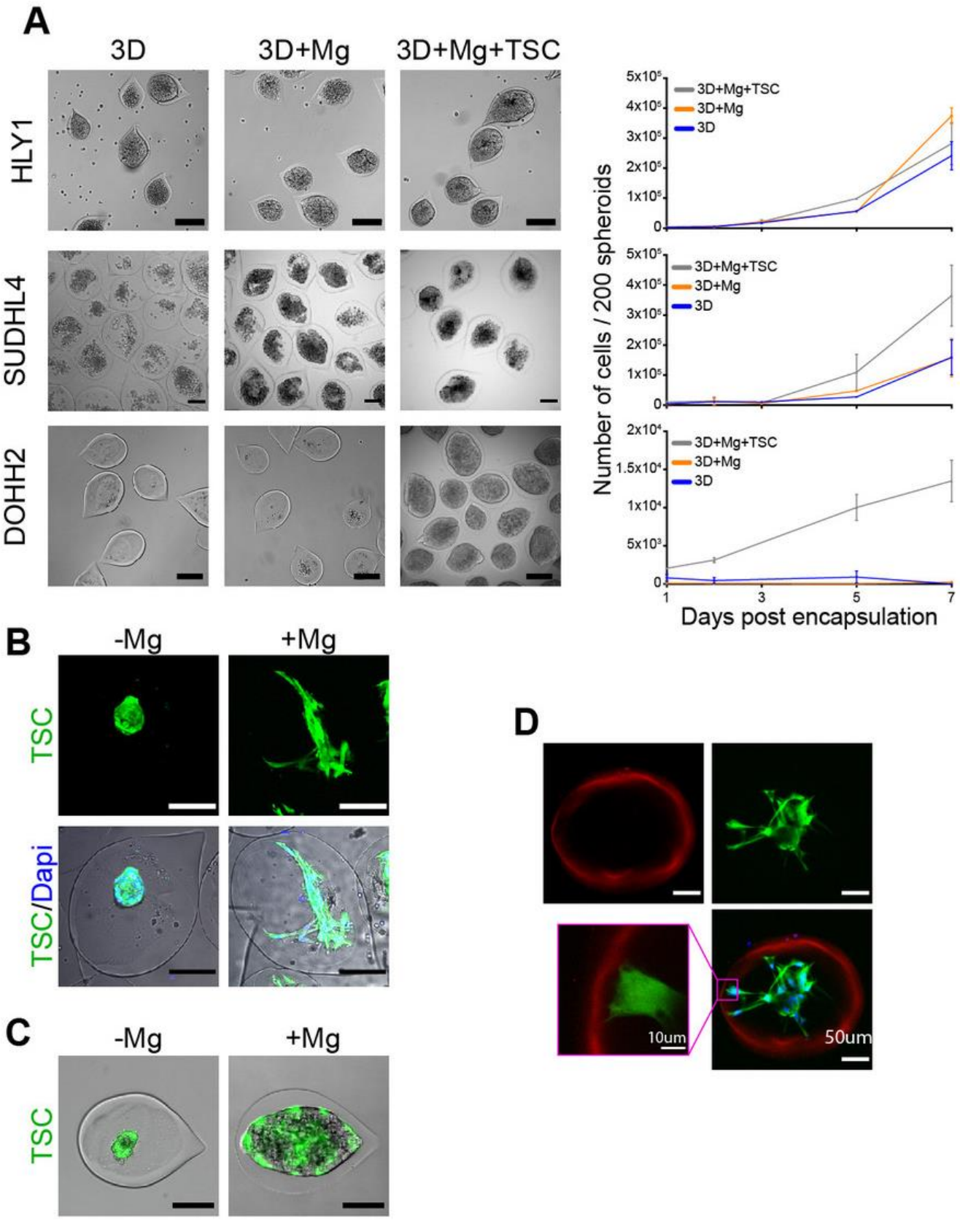
A
3D
3D+Mg
3D+Mg+TSC
HLY1
SUDHL4
DOHH2
Number of cells / 200 spheroids
Days post encapsulation
B
-Mg
+Mg
TSC
TSC/Dapi
C
-Mg
+Mg
TSC
D
10um
50um

Figure 4

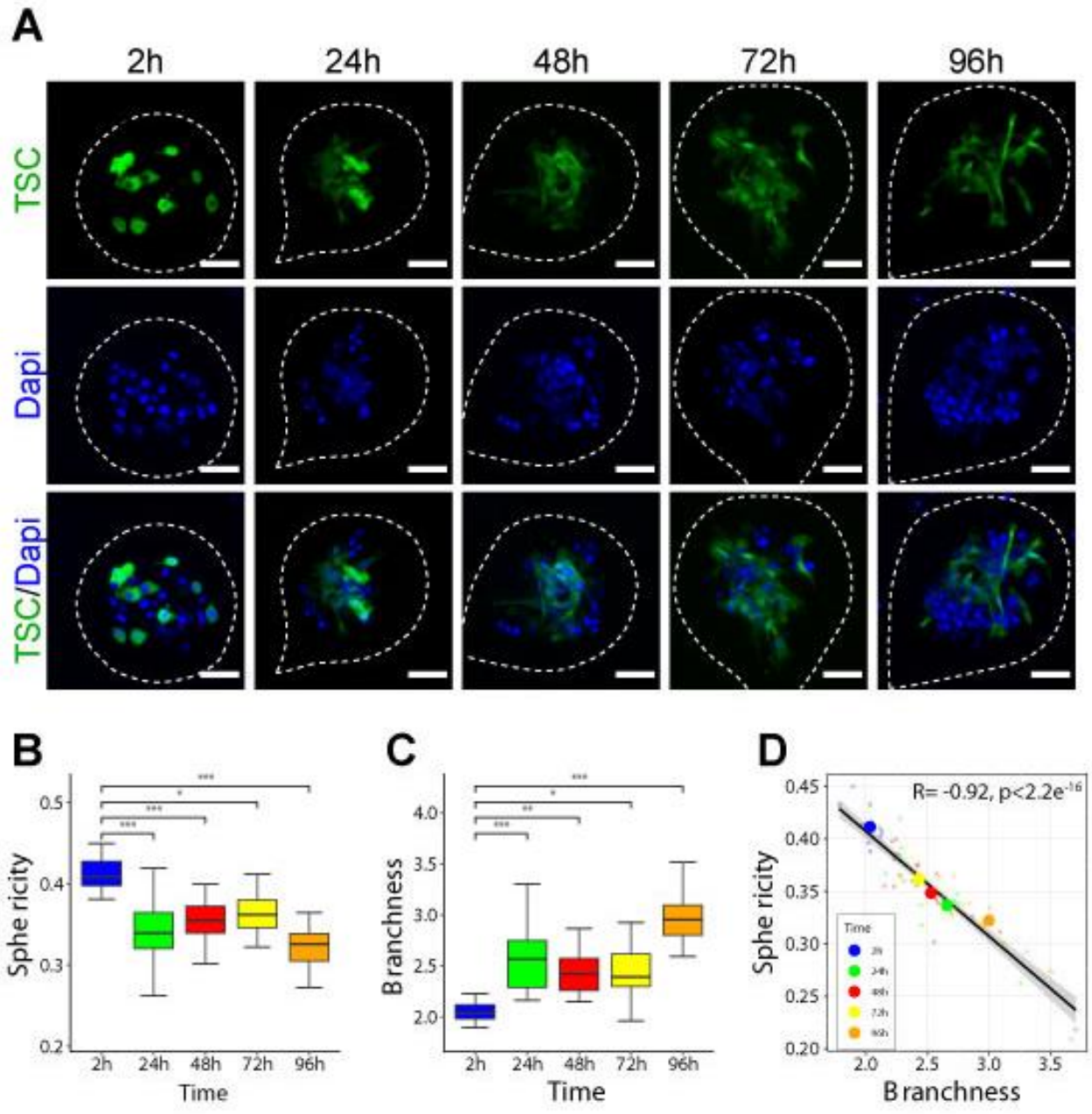
A
2h
24h
48h
72h
96h
TSC
Dapi
TSC/Dapi
B
Sphe ricity
Time
C
Branchness
Time
D
R= -0.92, p<2.2e-16
Sphe ricity
Branchness
Time

Figure 5

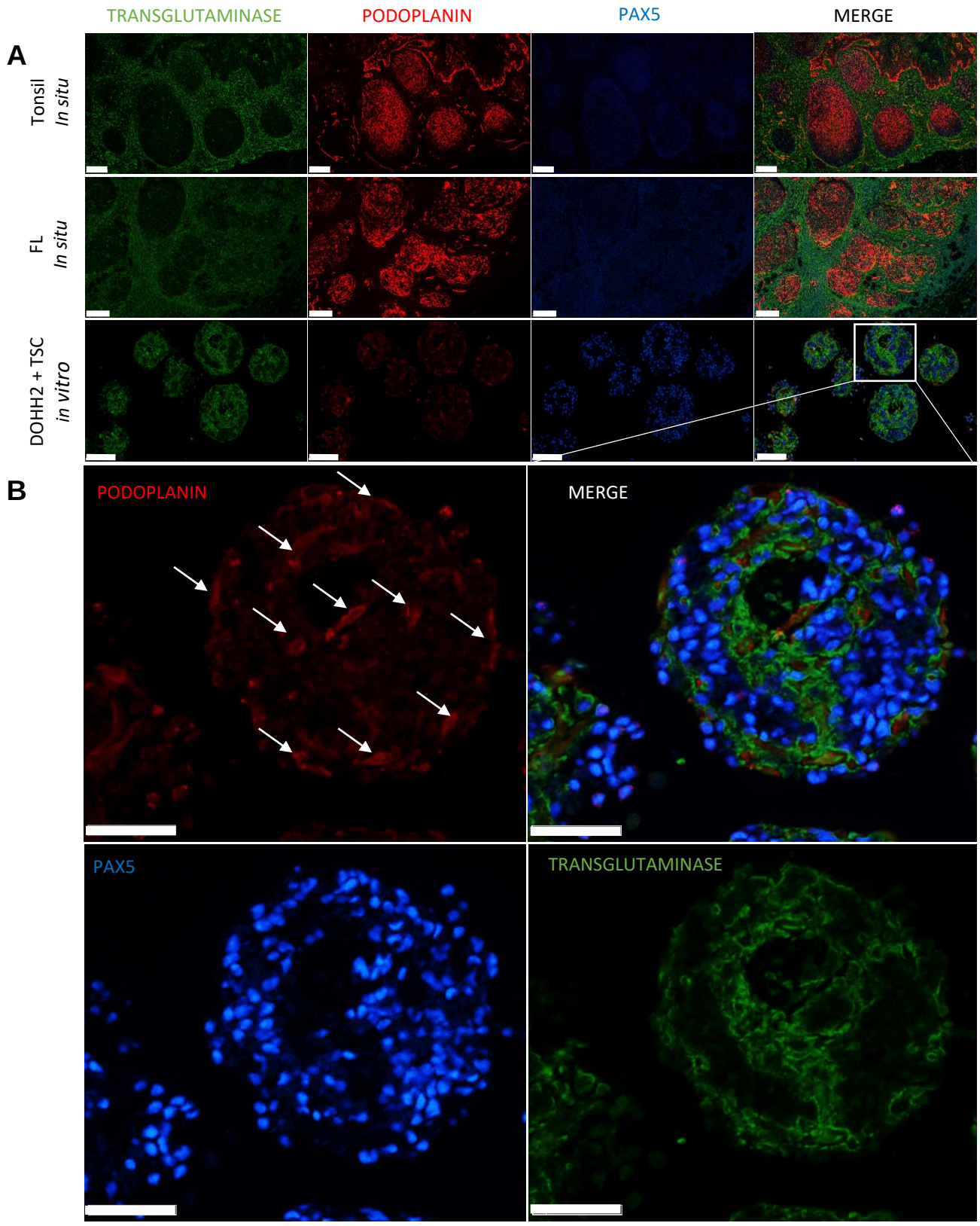
TRANSGLUTAMINASE
PODOPLANIN
PAX5
MERGE
A
Tonsil
In situ
FL
In situ
DOHH2 + TSC
in vitro
B
PODOPLANIN
MERGE
PAX5
TRANSGLUTAMINASE

Figure 6

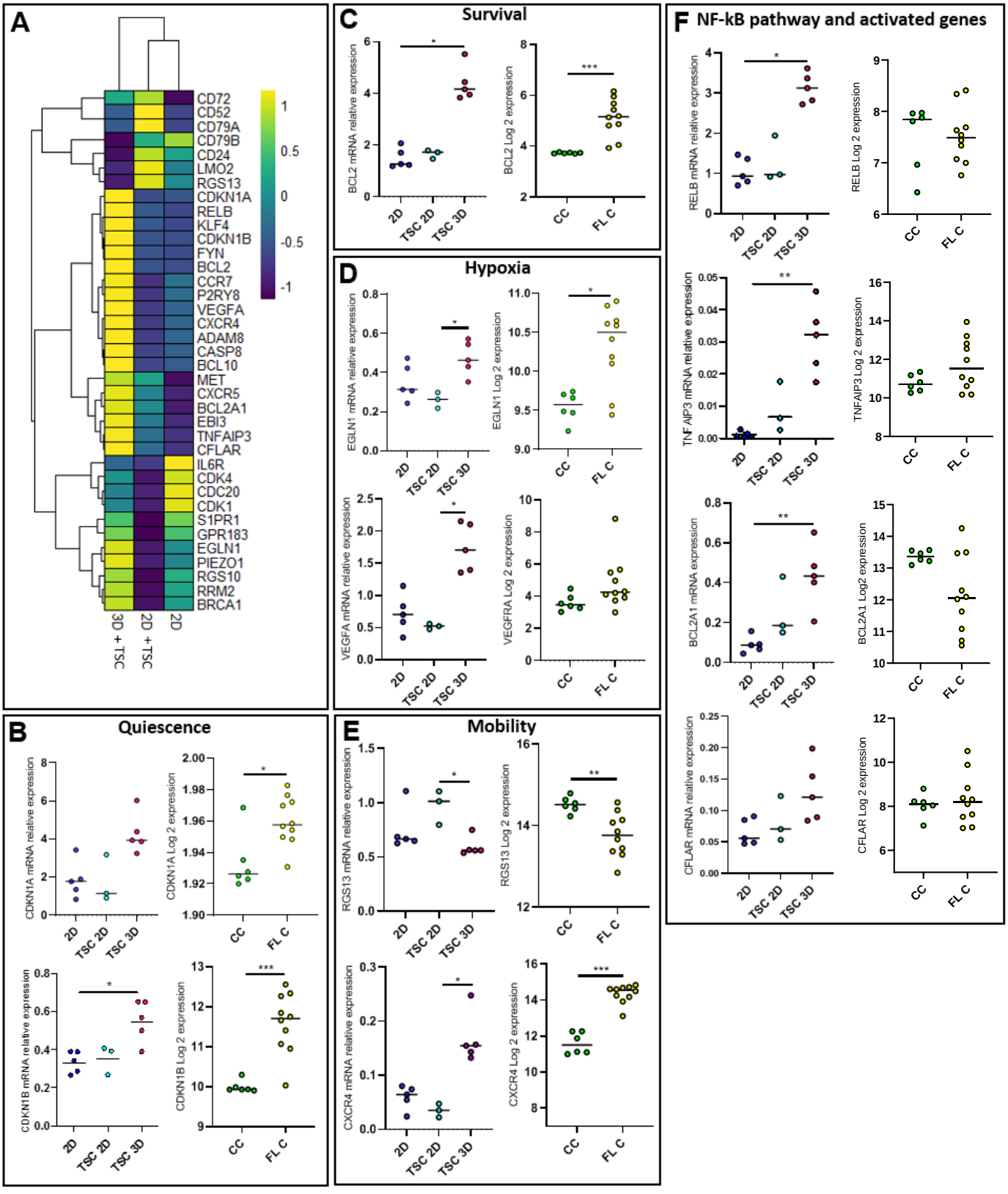
A
CD72
CD52
CD79A
CD79B
CD24
LMO2
RGS13
CDKN1A
RELB
KLF4
CDKN1B
FYN
BCL2
CCR7
P2RY8
VEGFA
CXCR4
ADAM8
CASP8
BCL10
MET
CXCR5
BCL2A1
EBI3
TNFAIP3
CFLAR
IL6R
CDK4
CDC20
CDK1
S1PR1
GPR183
EGLN1
PIEZO1
RGS10
RRM2
BRCA1
3D + TSC
2D + TSC
2D
1
0.5
0
-0.5
-1
B
Quiescence
CDKN1A mRNA relative expression
CDKN1A Log 2 expression
CDKN1B mRNA relative expression
CDKN1B Log 2 expression
2D
TSC 2D
TSC 3D
CC
FL C
C
Survival
BCL2 mRNA relative expression
BCL2 Log 2 expression
D
Hypoxia
EGLN1 mRNA relative expression
EGLN1 Log 2 expression
VEGFA mRNA relative expression
VEGFRA Log 2 expression
E
Mobility
RGS13 mRNA relative expression
RGS13 Log 2 expression
CXCR4 mRNA relative expression
CXCR4 Log 2 expression
F
NF-kB pathway and activated genes
RELB mRNA relative expression
RELB Log 2 expression
TNFAIP3 mRNA relative expression
TNFAIP3 Log 2 expression
BCL2A1 mRNA relative expression
BCL2A1 Log2 expression
CFLAR mRNA relative expression
CFLAR Log 2 expression

Figure 7

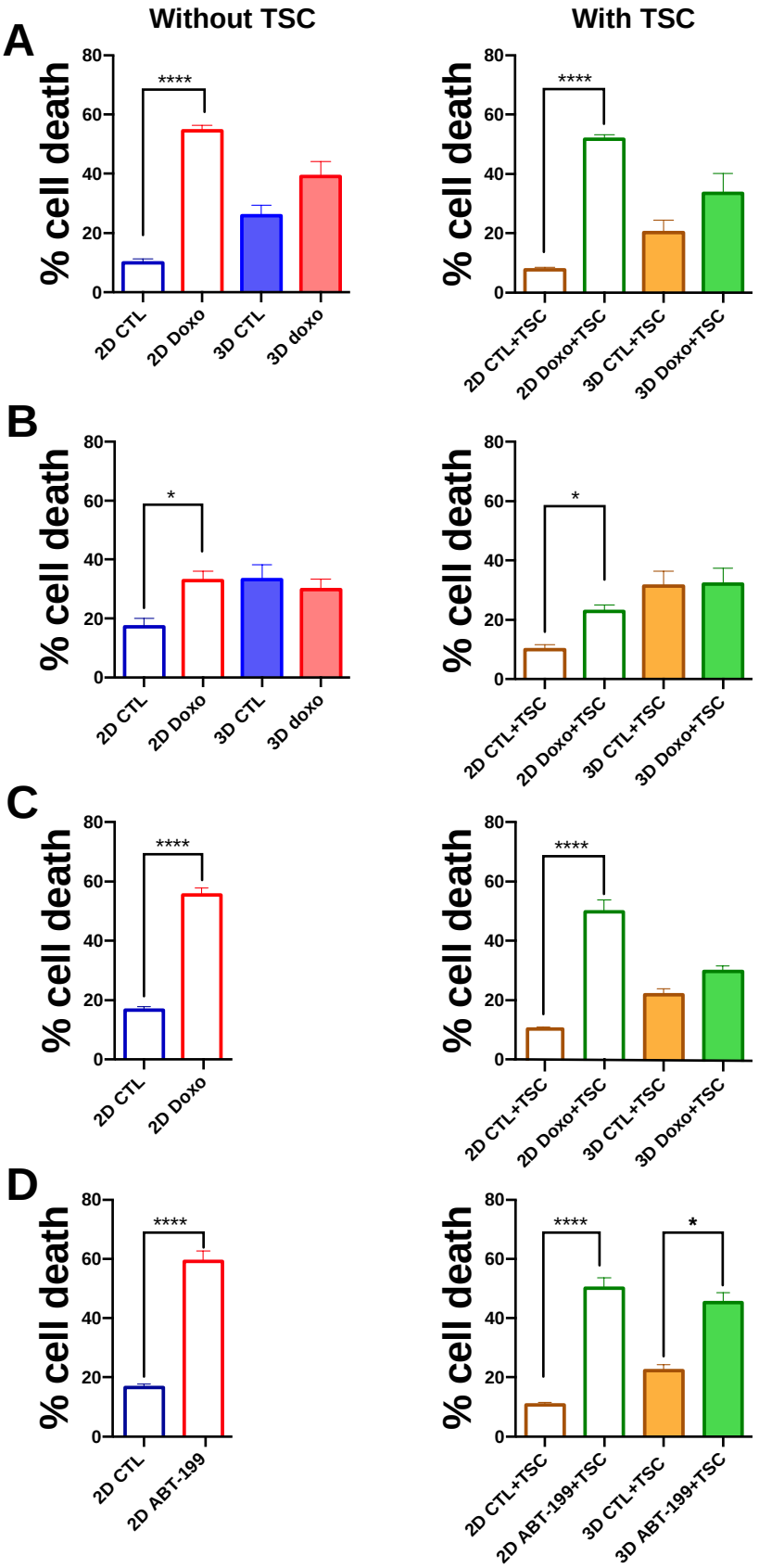
Without TSC
With TSC
A
B
C
D
% cell death
0
20
40
60
80
****
*
2D CTL
2D Doxo
3D CTL
3D doxo
2D CTL+TSC
2D Doxo+TSC
3D CTL+TSC
3D Doxo+TSC
2D ABT-199
2D ABT-199+TSC
3D ABT-199+TSC